

Beam optics studies for a uranium ion micro-beam

Brandon Rayhaun *

*University of Chicago, and Argonne National Laboratory

Submitted as a summary report at the conclusion of the 2014 Lee Teng summer internship at ANL

The proposed XMAT (eXtreme MATerials) facility at the Argonne Advanced Photon Source (APS) promises to advance our understanding of and aid in the development of advanced materials for fusion and fission reactor fuels and structural elements. An ion-beam accelerator for this facility is being designed by the nuclear physics accelerator group in the Argonne Physics Division. Ion energies on the order of ~ 1 MeV/u were chosen to create damage at a depth of 10 microns, far enough below the surface to affect the bulk material. By co-locating this accelerator at the APS, the XMAT facility will have the unique capability of in-situ 3D X-ray imaging of the material as the damage evolves in time. This sub-project is to design the focusing optics with the high accuracy needed to simulate a heavy ion micro-beam capable of delivering at least 10^7 ions per second into a 10 micron diameter spot. The plan is to use a superconducting solenoid to achieve an overall flux density increase of 100 times that at the linac output while maintaining a sufficiently large final working distance between the superconducting solenoid and the sample. High accuracy transfer maps using COSY Infinity and a custom-written ion tracking program have been shown to agree at the sub-micron level.

Introduction and preliminaries

The proposed eXtreme MATerials (XMAT) beamline for the Advanced Photon Source (APS) at Argonne aims to help in the development of radiation tolerant materials for nuclear environments. Damage from fission products in reactor fuels and neutrons in structural materials typically occurs over long periods of time, so an accelerator which is capable of delivering significant damage greater than 2500 displacements per atom in the solid (dpa, unit of damage) is needed to conduct studies within shorter time frames. The strategy is to take uranium ion or xenon beams produced from a linear accelerator at typical fission fragment energies and focus them using superconducting solenoids to achieve high particle densities at the sample being studied.

Apparatus. The main design of the beamline is shown in Fig. 1. The important features of the schematic are the heavy ion linear accelerator, a 100 μm -diameter aperture, a superconducting solenoid which achieves a magnification of $\sim \frac{1}{10}$, and a second solenoid which creates a suitable working distance between the sample and the optics in order to avoid subjecting the materials being investigated to large B fields.

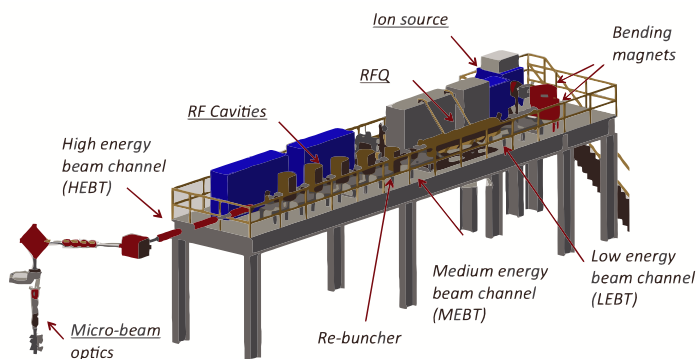


Fig. 1. Schematic of the XMAT beamline.

The work we are undertaking is the design of the micro-beam optics parameters. More specifically, the goal was to decide the relevant drift lengths (distance between the accelerator and the first solenoid, between the first solenoid and the second, etc.) and also the dimensions and strengths of the solenoids in order to optimize the amount of damage delivered. It is important to appreciate the fundamental principles underlying solenoid optics in order to understand our approach to solving this problem.

Solenoid optics. In introductory physics classes, students typically derive the magnetic field on axis for solenoids which are infinitely long. In this context, it is unclear how solenoids could be used for focusing at all. The answer lies in the details of solenoids' fringe fields.

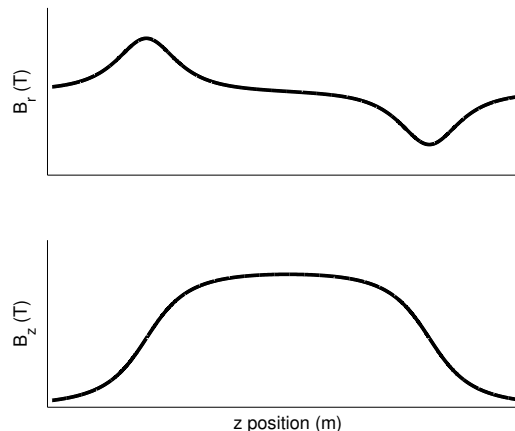


Fig. 2. Plot of the radial and axial components of the magnetic fringe field of a solenoid along a line parallel to its axis.

Basic principles

One can determine purely from symmetry arguments, namely that solenoids possess rotational invariance, that the radial component of the magnetic field vanishes along the axis. An ideal particle traveling along this axis thus will not experience any forces since

$$\vec{F} \propto \vec{v} \times \vec{B} = |\vec{v}| \hat{z} \times |\vec{B}| \hat{z} = 0.$$

However for a particle which travels at an offset from the axis, there will be a radial fringe field near the edges of the solenoid, as depicted in Fig. 2.

As the particle enters, the radial component of the field interacts with the \hat{z} component of the velocity, which delivers an angular kick to the particle so that its azimuthal velocity becomes nonzero. This component of the velocity is then allowed to interact with the axial field in the center of the solenoid, resulting in the increase of the radial component of the velocity. As the particle exits, the radial field, which is the same in magnitude as in the entrance but opposite in sign, cancels out the azimuthal component of the particle velocity that was acquired, but leaves the radial one. The net effect is that the particle will be deflected towards the axis, as observed in Fig. 3.

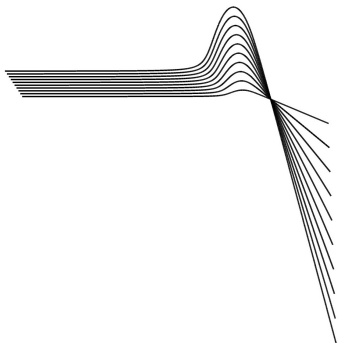


Fig. 3. Trajectories of particles traveling through a solenoid beginning at different radial offsets.

Abberations

Much of the work in designing optical components is evaluating and minimizing higher order aberrations which dominate the situation at hand. We identified two aberrations whose contributions to particle trajectories were non-negligible and focused on reducing their combined effect. These aberrations were due to contributions from $(\vec{x}|a^3)$ and $(\vec{x}|a\delta)$ terms (we will make the notation more precise for readers who are less familiar with it below). The limits on divergence and energy spread acceptance due to these aberrations were able to be determined independently.

Divergence aberration. There are three natural choices we will consider when it comes to positioning the sample: the image point, the position of maximum central areal density, and the circle of least confusion. It is entirely possible that the latter two coincide— this was not determined in our work, but will be investigated in the near future.

To define the first position, consider that, to first order, particles beginning on axis with small divergences will all intersect the axis at the same point. We will refer to this position as the image point. If we consider the density of particles very close to the z -axis, then the point at which this density is maximum is referred to as the position of maximum central areal density.

The circle of least confusion requires a bit more effort to define. If we factor in 3rd order aberrations, particles with large initial divergences will hit the axis at an earlier point on the axis than particles with small initial divergences, and thus will be displaced from the axis by the time they reach the image point. The circle of least confusion can loosely be

interpreted as the point at which the diameter of the beam spot is smallest (which will *not* be at the image point due to these aberrations).

To describe this quantitatively, let us adopt a convenient notation— In general, the final spatial coordinates, divergences, and deviations will be a function of the initial spatial coordinates, divergences, and deviations. We will write the coefficient in the Taylor expansion of the final particle parameter p_f which is associated with the product of initial parameters $q^1 \cdots q^n$ (note we may have $q^k = q^j$) as $(p_f|q^1 \cdots q^n)$. Formally then,

$$p_f = \sum_{n \in \mathbb{Z}, q^1 \cdots q^n} (p_f|q^1 \cdots q^n) q_i^1 \cdots q_i^n$$

For more information regarding this formalism, see [2]. Also, as a convenient shorthand, we adopt the notation

$$(\vec{x}|q^1 \cdots q^n) := ((x|q^1 \cdots q^n), (y|q^1 \cdots q^n))$$

and similarly for $\vec{a} = (a, b)$. We can then model the displacement in a monochromatic beam at the image point to third order like

$$r_f \approx |(\vec{x}|a^3)a_z^3|$$

where we have neglected to include second order contributions because of symmetry arguments. More generally, within a neighborhood around the image point, the radial displacement from the axis as a function of z can be modeled approximately by

$$r_f(z) \approx |(\vec{x}|a)_z a_i + (\vec{x}|a^3)_z a_i^3|$$

where we can then take as a definition of the image point the value of z for which $(\vec{x}|a)_z = 0$. The aberration coefficient at the image point, $(\vec{x}|a^3)_{image}$, is affected by various solenoid parameters (for instance, it is typically reduced by taking the solenoid radius to be larger). Part of our objective was to minimize this aberration coefficient without driving up costs too much.

For a particular maximum divergence acceptance, a_{max} , the point at which image diameter is minimum turns out not to be the image point. In fact, it occurs slightly before the image point, and can be determined by finding the value of z which minimizes the expression

$$\sup_{|a_i| \leq a_{max}} |(\vec{x}|a)_z a_i + (\vec{x}|a^3)_z a_i^3|.$$

Moving the sample from the image point to the circle of least confusion can lead to better amplification, as visualized in Fig. 4.

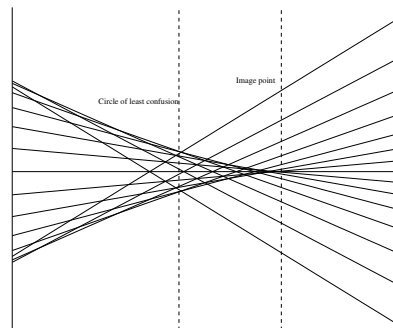


Fig. 4. Motion in the \hat{x} - \hat{z} plane of particles of various divergences reaching the end of the focusing stage. The circle of least confusion and image point are separated by ~ 1 mm.

Chromatic aberration. The chromatic aberration arises from a combination of initial divergence and energy spread of the accelerator. If we work to second order, then the displacement of a particle with initial divergence a_i and energy deviation $\delta_i := (E_i - E_0)/E_0$, where E_0 is the initial energy of the reference particle, is

$$r_f(z) \approx |(\vec{x}|a)_z a_i + (\vec{x}|a\delta)_z a_i \delta_i|.$$

We used the contribution of the chromatic aberration on image size to determine the maximum allowed energy spread in the uranium ion accelerator.

Methods

We opted to use COSY Infinity as our main computing tool because it provided exceptionally fast and extensive libraries for computation of accelerator transfer matrices and because the differential algebraic techniques on which it is based allowed us to quantitatively investigate the effect of various aberrations. However, since the goal beam size at the sample was $\sim 10 \mu\text{m}$, it was unclear that COSY 1) possessed particle integration of fine enough temporal resolution to achieve micron level precision, 2) faithfully reproduced a solenoid’s magnetic induction with its differential algebraic methods, or 3) appropriately coped with the sample being placed in a location with nonvanishing magnetic field. For verification purposes, we created a custom program written in MATLAB for computing particle trajectories through the solenoid which gave us complete control over the integration step size and B -field computation accuracy.

Computing particle trajectories in MATLAB. Our custom program adopted a very simple, yet powerful strategy. The computation of solenoidal magnetic fields was based on the elliptical integral formulation discussed in [1] and the particle trajectories were computed using a temporal integration scheme.

Solenoidal field computation

Built in functions in MATLAB allowed us to compute elliptical integrals to arbitrary accuracy. In terms of these integrals, the field of a finite, thin solenoid at any point in space, (r, θ, z) is

$$B_r = \frac{\mu n i}{\pi} \sqrt{\frac{a}{r}} \left[\frac{2 - k^2}{2k} K(k) - \frac{E(k)}{k} \right]_{\xi_-}^{\xi_+}$$

$$B_z = \frac{\mu n i}{4} \left[\frac{\xi k}{\pi \sqrt{ar}} K(k) + \frac{(a - r)\xi}{|(a - r)\xi|} \lambda_0(\phi, k) \right]_{\xi_-}^{\xi_+}$$

where a is the coil radius, K and E are elliptic integrals of the first and second kind, $k = \sqrt{4ar/[\xi^2 + (a + r)^2]}$, L is the coil length, n is the number of turns per unit coil length, λ_0 is the Heuman lambda function, $\xi_{\pm} = z \pm \frac{L}{2}$, and $\phi = \tan^{-1} |\xi/(a - r)|$. Thick solenoids were approximated by superposing several thin solenoids of various coil radii. B fields computed using MATLAB were found to match with those computed using COSY to the Gauss level— since the scale of the problem is around $\sim 5\text{T}$, the correspondence was $\sim 1/50\%$.

Particle integration

Once we were able to determine the magnetic field due to an arbitrary assortment of solenoids, we were able to write a program to compute particle trajectories. Given some initial

coordinates and velocity, \vec{x}_i and \vec{v}_i , of a particle at time t_i with mass m and charge q , we computed \vec{x}_f and \vec{v}_f in the next time stamp, $t_f = t_i + \Delta t$:

$$\vec{x}_f = \vec{x}_i + \Delta t \vec{v}_i, \quad \vec{v}_f = \vec{v}_i + \Delta t \frac{q}{m} \vec{v}_i \times \vec{B}(\vec{x}_i)$$

where non-relativistic equations were used because particle energies were small enough that speeds were always $< .05c$. Iterating this procedure, we were able to capture full particle trajectories, which were found to correspond to those computed in COSY to order ~ 2 microns if the integration step size was chosen sufficiently small in MATLAB and the order of the maps sufficiently large in COSY.

Goals and design considerations. In designing the optics of the accelerator, there were several specifications we hoped to achieve.

Size. It was a major objective that the XMAT ion accelerator system should not occupy too much space. This consideration factored in to our decision of whether to use one or two solenoids for focusing.

Sample distance from solenoid. We strove for a design in which the circle of least confusion was far enough from the edge of the optics that the B field produced there would be negligible, ensuring that the damage to the sample material would not be altered by the presence of strong magnetic fields.

Beam degradation. We sought to maximize our energy deviation, divergence, and displacement acceptances as much as possible in order to keep as much of the original beam from the linac output as possible.

Magnification. The primary goal was that the optics focus the beam from the linac output down to $1/10$ its initial size.

Cost. Another factor that contributed to our design was that two solenoids would inevitably cost more than one. We additionally sought to choose the strength and dimensions of the solenoid so that its price was minimized.

We used the FIT procedure in COSY extensively on various parameters of the system in order to achieve these goals. We optimized with respect to solenoid radius, length, and current as well as all the relevant drift lengths in the problem so that

$$|(\vec{x}|x)| = |(\vec{x}|y)| \approx \frac{1}{10}, \quad \text{and}$$

$$\sup_{|a_i| \leq a_{max}} |(\vec{x}|a)_z a_i + (\vec{x}|a^3)_z a_i^3| \text{ is small for } a_{max} = 3 \text{ mrad}$$

or, in words, that the magnification be approximately $\frac{1}{10}$, and the circle of least confusion be minimized.

Results

Our methods above produced a working first order design for the first stage of the optics system. A second stage will ultimately be needed in order to focus the particles farther away from the edge of the solenoid because the first stage provides a working distance of only 30 cm between the sample and the optics, which subjects the material being investigated to large B fields, on the order of $\frac{1}{10}$ T. However, many properties of the first solenoid can be studied in their own right, and even inform future direction.

Our original goal was to design a system capable of delivering a $100\times$ flux density increase between the linac output and the sample. In the ideal case that the linac outputs particles of zero energy deviation, we were able to achieve an increase of $\sim 90\times$. Accounting for the energy spread at the accelerator reduces this number, but in the last section, we propose a method for improving the design.

Accelerator output. To begin our analysis, we needed to determine the distribution of particle positions and divergences at the beginning of the optical system. Our data consisted of information about 1906 particles at the linac output. The distribution of energy deviations was approximately uncorrelated with the distributions of positions and divergences (a maximum correlation of .04), so we were able to consider effects from energy spread separately when needed.

We fit a multivariate normal distribution to this (x, a, y, b) data, whose mean and covariance we will refer to as (μ_i, Σ_i) . From here, we were able to numerically compute the fraction of particles produced at the linac output that would make it through the $100 \mu\text{m}$ -diameter aperture, which was 2.3×10^{-4} . We set our goal of a $100\times$ increase in flux density because we originally estimated that the fraction of particles traveling through the aperture would be $\sim 10^{-4}$. Since we have roughly $2.3\times$ as many particles as we guessed we would have, we can settle for a more modest flux density increase of $\sim 45\times$ between the aperture and the sample.

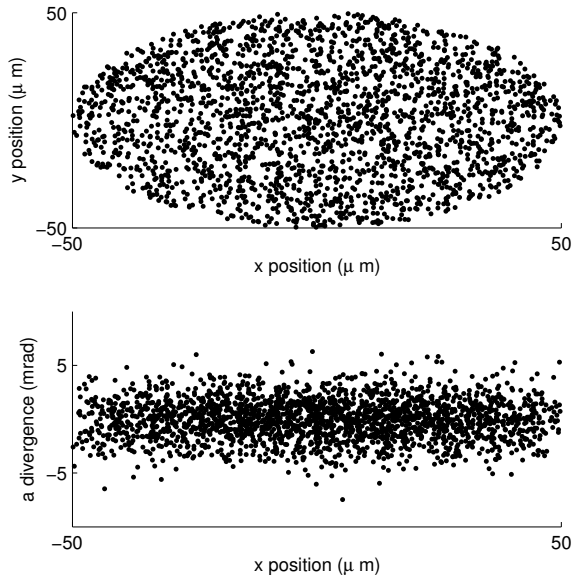


Fig. 5. The first plot depicts the spatial coordinates of a sample of particles entering the optical system. Note how the distribution is nearly uniform as a result of the aperture selecting only particles well within the portion of the distribution where the pdf is nearly constant.

The second plot depicts the coordinates of particles in phase space. The distribution in divergence is approximately Gaussian.

For the remainder of our simulation, we generated the particles which would be fed into the optical system by using a random number generator which sampled from the distribution $\mathcal{N}(\mu_i, \Sigma_i)$, and tossed out all those particles which had $r = \sqrt{x^2 + y^2} > 50 \mu\text{m}$, i.e. tossed out all particles which did not make it through the aperture. When we wished to simulate the effects of energy spread, we assumed the energy deviations, δ , followed a normal distribution $\mathcal{N}(0, \sigma_\delta^2)$. These results are summarized in Fig. 5.

Optics output. After obtaining the distributions of particles entering the optics system, we were able to compose them with the transfer map of the optimized system computed in COSY

to obtain the particle coordinates at the sample, displayed in Fig. 6.

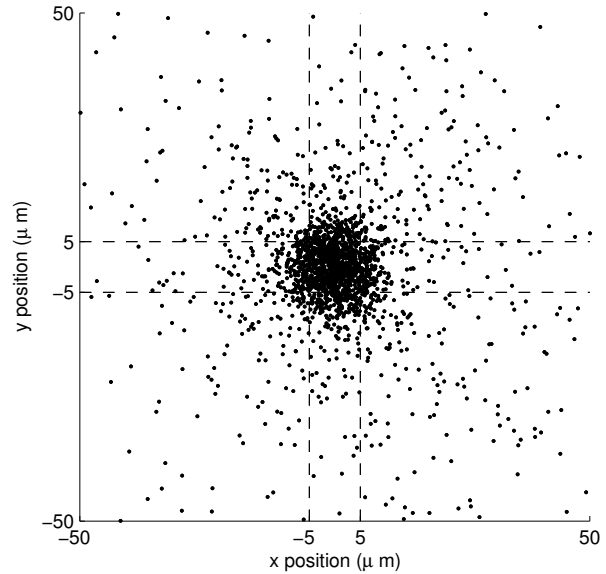


Fig. 6. A plot of the spatial coordinates of particles that have reached the sample. Approximately $\frac{1}{4}$ of the particles that make it through the aperture arrive within a $5 \mu\text{m}$ circle. In these simulations energy spread is assumed to be negligible.

The most important measure of how well the optics are working is how densely packed the particles are in the very center of the sample material, especially since the photons from the APS will only be imaging a very small area. Defining the magnification $M(r)$ as the density of particles in a circle of radius r at the sample divided by the density of particles at the $100 \mu\text{m}$ -diameter aperture, the maximum value of the magnification is the appropriate measure of performance.

From Fig. 7, we see that the maximum magnification achieved is about 40, which multiplied by the $2.3\times$ extra number of particles we have gives us a flux density increase of $\sim 92\times$, which is close to our desired goal.

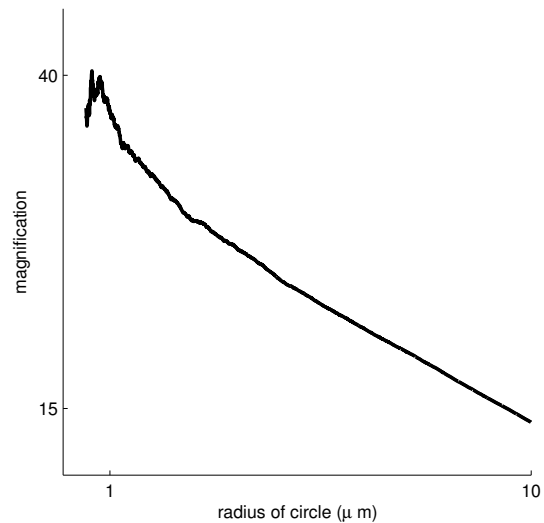


Fig. 7. A plot of the magnification of our system as a function of the circle size we are considering. Again, energy spread is assumed to be negligible in these simulations.

Discussion and future direction

Although we came close to achieving our goal in the case of negligible energy spread, we can do much better as a whole. The location of the circle of least confusion is heavily dependent on the distribution of energy, spatial coordinates, and divergences at the linac output. Our original optimization conditions, discussed in the section “Goals and design considerations,” did not take energy spread into account, or even the Gaussian nature of the distribution of divergences at the linac output. With more care, better optimization conditions can be chosen to cater to the specifics of the accelerator properties.

1. E. Callaghan and S. Maslen, The magnetic field of a finite solenoid, Technical Note D-465, (1960).
2. M. Berz and K. Makino, COSY INFINITY 9.1 Beam Physics Manual, MSU Report

Work will also be done on designing the second stage optics. Additional focusing in the second stage could be used to increase performance substantially.

Acknowledgements

I’d like to thank Jerry Nolen for mentoring me during my stay at Argonne and supervising my work on this project. I’d also like to thank Shashikant Manikonda for helping me become better acquainted with the software I needed for this work. Finally, I’d like to thank Eric Prebys and Linda Spentzouris for organizing the Lee Teng internship which allowed me to complete this work in the first place.

MSUHEP 060804-rev, (2013).

3. <http://www.ne.anl.gov/xmat/>